Integrated 3D modeling unravels the measures to mitigate nickel migration in solid oxide fuel/electrolysis cells

Jiao, Zhenjun; Su, Yunpeng; Yang, Wenyue; Zhou, Jianli; Zhang, Jin; Tong, Xiaofeng; Shang, Yijing; Chen, Ming

Published in:
Journal of Materials Chemistry A

Link to article, DOI:
10.1039/d3ta06563d

Publication date:
2024

Document Version
Peer reviewed version

Integrated 3D Modeling Unravels the Measures to Mitigate Nickel Migration in Solid Oxide Fuel/Electrolysis Cells

Zhenjun Jiao*[a], Yunpeng Su[a,1], Wenyue Yang[a], Jianli Zhou[a], Jin Zhang[a], Xiaofeng Tong[c,b], Yijing Shang[b], Ming Chen*[b]

a. *School of Science, Harbin Institute of Technology (Shenzhen), Shenzhen 518055, China*

b. *Department of Energy Conversion and Storage, Technical University of Denmark, 2800, Kgs. Lyngby, Denmark*

c. *Institute of Energy Power Innovation, North China Electric Power University, Beijing 102206, China*

1. *Co-first authors of the article*

Abstract

Numerical modeling plays an important role in understanding the multi-physics coupling in solid oxide fuel/electrolysis cells (SOFCs/SOECs) operated at elevated temperatures. During long-term operation of SOFCs and SOECs, cell durability is limited by nickel (Ni) morphological changes and migration. To reveal the mechanisms behind these phenomena, a unified numerical model utilizing the phase-field (PF) method is integrated with a finite element (FE) multi-physics coupled heterogeneous single-cell model to quantitatively investigate the microstructure evolution of hydrogen electrodes operated in different modes. Based on the 3D microstructures of single-cell components reconstructed using the focused ion beam-scanning electron microscopy technique (FIB-SEM), the performances of different cells and the corresponding microstructure evolutions caused by Ni coarsening and migration can be simulated under an identical framework in the FC and EC modes, taking into account the complex multi-physics coupling effects. It is shown that, in addition to conventional interfacial energies, the Ni migration driven by the electrochemical potential gradient induced by current also plays an important role during the microstructure evolution. The integrated model is also applied to the simulation of the microstructure evolution of the Ni-YSZ hydrogen electrode infiltrated with GDC nanoparticles to interpret its positive effect on the improvement of the electrode durability.

Keywords: Integrated modeling, SOFC/SOEC, Multi-physics, Finite element method, Phase-field method, Ni migration;

1. Introduction

Solid oxide fuel/electrolysis cells (SOFCs/SOECs) have attracted tremendous interest due to their promising potential for reversible conversion of chemical and electrical energy [1]. However, the limited long-term durability of these cells remains a major challenge to their commercialization [2, 3]. Currently, Ni-yttria-stabilized zirconia cermets (Ni-YSZ) are utilized in most SOFCs/SOECs as composite hydrogen electrode materials. Although these Ni-YSZ electrodes exhibit excellent activity in both FC and EC modes, their stability properties differ significantly and show considerable degradation during continuous operation at high current densities [4–7]. In our previous work [8], the initial performance and degradation of an SOFC operated over 7000 hours were analyzed, which clearly showed the phenomenon of ionic current concentrating at electrolyte, caused by Ni coarsening and accumulation toward electrolyte, dominated the degradation of the cell. The work of Sun et al. [9] compared the initial and final performances of a SOEC after long-term operation over 4000 hours, and the results demonstrated that the degradation of the cell was dominated by the microstructural changes of Ni-YSZ electrode based on post-mortem analysis.

Redistribution of Ni, including coarsening and migration of Ni, has been recognized as a major contributor to the degradation by impacting the ionic and electrical conductivities and active triple-phase-boundaries (TPBs) in the hydrogen electrode, which causes the performance degradation of the cells.[10–13]. It is well known that Ni coarsening occurs during operation in FC and EC modes and under open circuit voltage (OCV) condition [14–16].There are few works dealing with the investigation on Ni migration in the FC mode. Menzler et al. reported the phenomenon of Ni migration toward the electrolyte in an SOFC after more than 10 years of operation [17]. In contrast, Ni migration away from the electrolyte was frequently observed during EC operation under strong polarization, but not under OCV conditions [13, 18]. Recently, we investigated the morphological changes occurring on patterned Ni film electrodes during operation in FC and EC modes [19–21]. We attempted to explain the phenomena by establishing a correlation between the wettability of Ni on YSZ and the degree of adsorbed oxygen on the Ni surface. This indicates a strong

Email addresses: jiaozhenjun@hit.edu.cn (Zhenjun Jiao*[a]), minc@dtu.dk (Ming Chen*[b])

correlation between the degradation behavior and the overpotential experienced. Recently, some efforts have been made to elucidate the mechanism underlying Ni migration, but it remains elusive. For example, Mogensen et al. [18] proposed that Ni migrates in the form of $Ni(OH)_x$ species. However, we recently observed Ni migration during the EC operation of CO_2, suggesting that the $Ni(OH)_x$ species may not be the main contributor to Ni migration [14]. Cheng et al. [22] proposed theory based on a hypothesis, that the dynamic redox of Ni, combined with the coarsening and gas transport processes, could be related to Ni migration. However, the 1D steady-state model proposed showed limitations, mainly regarding the lack of the description of the microstructure of electrode and the consideration on transient effect of charge transport. So far, it is clear that the migration of Ni, either toward or away from the electrolyte, appears to be governed by a combination of complex mechanisms during long-term operation in a particular mode. Experiments have shown that Ni migration at relatively high current densities depends on the electrochemical process, while no migration is expected at low current densities [18]. These phenomena were explained by the assumption that migration is driven by the contact angle gradient of Ni on YSZ, which correlates with the electric potential gradient and/or the oxygen partial pressure gradient.

Given the time-consuming and costly nature of durability testing, as well as the potential for observational error in ex-situ experiments, numerical studies have become increasingly important in investigating the mechanisms of Ni redistribution. In recent years, various numerical methods such as the lattice Boltzmann method (LBM) and the finite element method (FEM) have been used in the study of multi-physics coupling for SOCs [8, 23–28]. In addition to these approaches, the phase-field method (PFM) has been shown to be a powerful simulation tool for predicting the microstructural evolution of hydrogen electrodes. Wang et al.employed [29] a combination of LBM and PFM to simulate the effects of Ni depletion on cell performance during EC operation. Their results showed that Ni depletion exacerbated the coarsening of Ni and lengthened the ion transport pathway, leading to an increase in activation overpotential. Lei et al. [30, 31] employed the PF method to simulate Ni migration and found that neither the $Ni(OH)_x$ species nor the contact angle gradient of Ni on YSZ, which can be affected by gas partial pressure alone, can serve as

sufficient driving forces for Ni migration. Rorato et al. [32] combined an electrochemical model with the PF model to simulate Ni migration in both FC and EC modes. Their model considered that the contact angle gradient of Ni on YSZ was influenced not only by the gas partial pressure, but also by the presence of oxygen vacancies at the Ni-YSZ interface related to the overpotential of the hydrogen electrode. Nevertheless, no clear explanation or accurate numerical modeling was proposed to reproduce the phenomena of Ni migration in different modes considering the complex effects of multi-physics coupling, which made it difficult provide theoretical guidance for improving cell performance and stability. At the current stage, most studies analyzed Ni migration qualitatively, while achieving real-time coupling between electrochemical and thermodynamic models remains a major challenge in a quantitative simulation. Therefore, limited progress has been made in the microstructural optimization of hydrogen electrode to prolong its performance stability and durability without accurate theoretical guidance.

Based on previous studies, we present a unified numerical modeling framework for simulating Ni migration in hydrogen electrodes in both FC and EC modes in this work. Taking into account the complex real-time multi-physics coupling effects between electrochemical and thermodynamic models, for the first time we achieved real-time integrated modeling of the hydrogen electrode microstructure evolution during operation. Integrated modeling involving FEM and PFM is performed based on real 3D microstructures reconstructed using the focused ion beam-scanning electron microscope (FIB-SEM) dual-beam technique [20, 33], with the goal of providing a fundamental understanding of the underlying mechanisms of Ni migration during operation in different modes. Based on the integrated modeling framework proposed, the infiltration of nano-sized GDC particles in hydrogen electrode to improve SOEC durability by inhibiting Ni migration was analyzed and quantitatively interpreted based on simulations.

2. Experimental

2.1. Electrochemical Performance Test

SOCs built with a Ni-YSZ hydrogen electrode as the support structure have the advantage of low ohmic resistance due to electrolyte thickness, which allows lower operating temperature and higher performance. 8YSZ (8 mol% yttria-doped zirconia) and 3YSZ are conventionally utilized in the functional layer (FL) and the supporting layer (SL) of hydrogen electrode, respectively, due to their high ionic conductivity and mechanical strength. In this work, two types of hydrogen electrode-supported SOCs were tested during long-term operation in either FC or EC mode. The first type is of a commercial SOC composed of a Ni-3YSZ hydrogen electrode support layer (HSL), a Ni-8YSZ hydrogen electrode functional layer (HFL), an 8YSZ electrolyte, a gadolinium-doped ceria (GDC) barrier layer (BL), and a lanthanum strontium cobalt ferrite (LSCF) oxygen electrode. The second type is of self-manufactured SOC composed of a Ni-3YSZ HSL, a Ni-8YSZ HFL, an 8YSZ electrolyte, a GDC-BL, and a GDC-LSCF composite oxygen electrode. The two types of SOCs were designated as cells A and B in this work. To investigate the influences of operation modes on Ni migration in Ni-YSZ hydrogen electrodes, samples of cells A and B were taken before and after long-term operation in FC and EC modes, respectively. Cell A was sampled after operation from the center of a short stack operated at a current density of 0.3 A cm^{-2} in H_2 humidified with 6% H_2O as fuel and air as oxidant at 1023 K for 7000 hours. For cell B, the sample was taken after operation from a sing-cell test with a current density of -1 A cm^{-2} in H_2 humidified with 50% H_2O at 1073 K for 1000 hours.

2.2. FIB-SEM Technique

The SEM images of the cross-sections of cells A and B before and after long-term operation are shown in Fig. 1(a)-(d) and compared. The phenomena of Ni accumulation toward the electrolyte with enhanced Ni-YSZ interface in FC mode and the opposite Ni migration away from the electrolyte in EC mode are clearly observed. Coarsening of Ni can also be observed in both HSL and HFL after operation in both modes. To facilitate subsequent numerical simulations, the initial microstructures of cells A and B before operation

were reconstructed using the FIB-SEM (Carl Zeiss, Crossbeam 350) dual-beam technique. The samples were infiltrated with low viscosity epoxy resin in a low pressure atmosphere to facilitate the segmentation of different phases. The cured samples were polished using an Ar-ion beam cross-section polisher (JEOL Ltd, SM -09010), and the series of FIB-SEM images were filtered and aligned using ImageJ software. The microstructures were then reconstructed in 3D by stacking the segmented image sequence. Based on the 3D reconstructions, adaptive tetragonal meshes were generated in MATLAB and imported into COMSOL for FE simulations; details of the 3D reconstruction can be found in Ref. [8].

3. Results and discussion

3.1. Scheme

The scheme of integrated modeling in this work is shown in Fig. 2(a). The microstructures of cells A and B were first reconstructed in 3D with a voxel length of $l_0 = 39.1$ nm. To simulate the evolution of the Ni-YSZ hydrogen electrode microstructure under complex coupling effects among conductions, electrochemical reactions, and mass transfer processes, a multi-physics coupled FE model was integrated with a PF model via the 3D microstructure reconstruction in a full-cell scale. In-house codes were developed for integrated simulation with automatic feature recognition, equation assignment, and subsequent numerical solution, linking MATLAB and COMSOL softwares. Adaptive tetrahedral meshes were generated in MATLAB and then imported into COMSOL. The FE modeling was first performed to predict the experimental electrochemical performances of a cell at full-cell scale to validate the model in the appropriate mode. The 3D multi-physics field data generated in the FE simulation, such as gas concentrations and electrochemical potential distributions in solid phases, were then extracted and imported into the subsequent PF model by projecting them onto the corresponding OP matrices using the k-nearest neighbors algorithm. The full-cell reconstruction with the hydrogen electrode after evolution predicted utilizing PFM was converted to adaptive tetrahedral meshes to update the microstructure for the FE simulation. The cyclic process was repeated to complete the integrated numerical simulation. Details of the FE and PF models are described

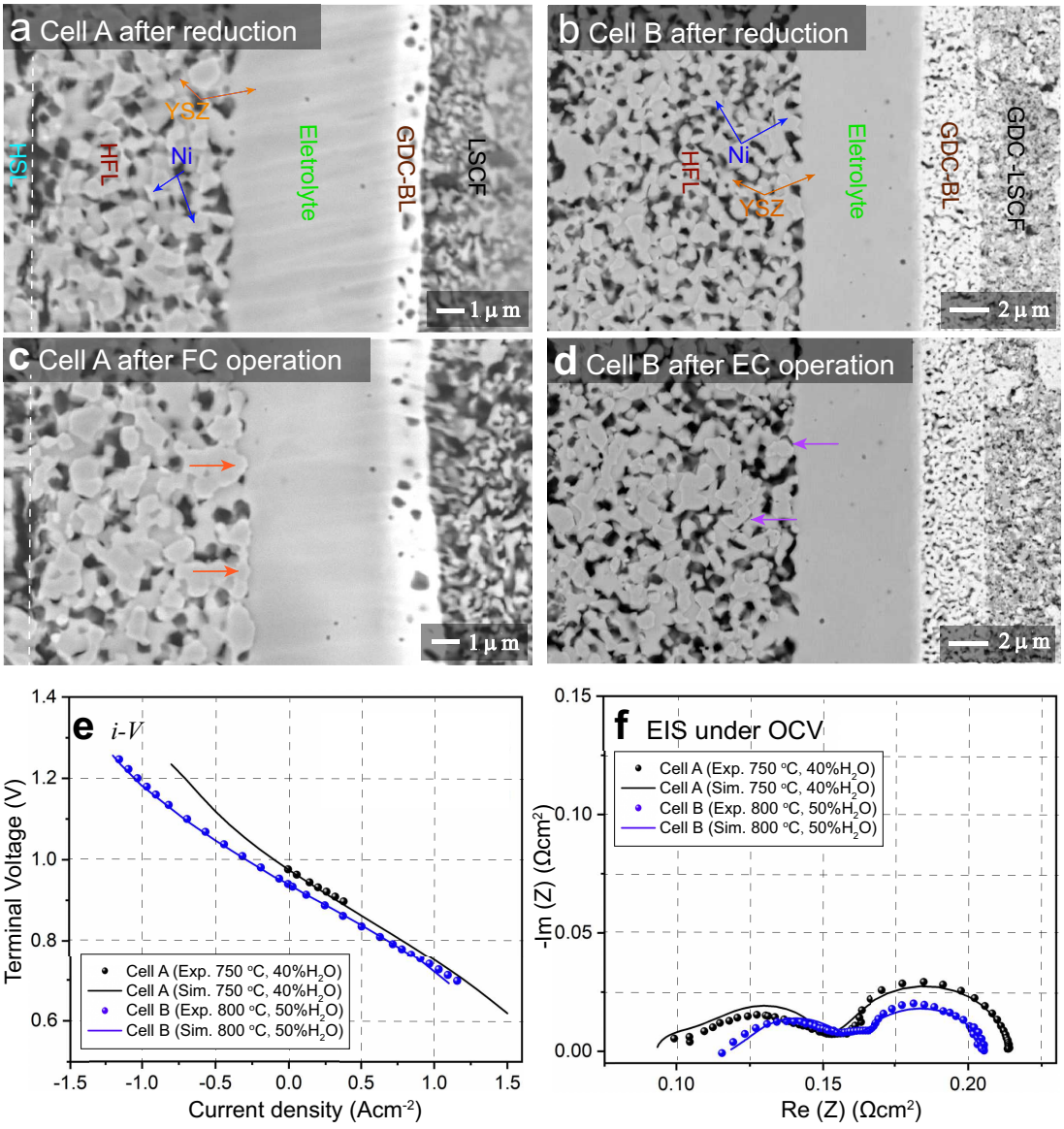

Figure 1: SEM images of single-cell cross-section for cell A (a) before and (b) after long-term FC operation, and cell B (d) before and (d) after long-term EC operation. Comparison between simulation and experimental results of (e) *i-V* and (f) EIS for cells A and B.

in Supporting Information.

3.2. FE simulations

For FE modeling, further details of parameters and empirical formulas can be referred to our previous work in Ref. [8]. In this work, the performances of cell A operated in FC mode and cell B operated in EC mode were simulated under the unique framework based on the 3D reconstructions of the full cell. To validate the modeling of FE, the initial performances in terms of current density-voltage relationship (i-V) and electrochemical impedance spectroscopy (EIS) were simulated using the environmental parameters presented in the experimental section for both cells. The corresponding simulation results of i-V and EIS were compared with the experimental data, as shown in Fig. 1(e) and f. It is clearly seen that the actual experimental data can be well reproduced in the simulations.

To facilitate later PF simulations of microstructure evolution in hydrogen electrodes during long-term operation, further simulations were performed using cells A and B under different conditions in FC and EC modes, respectively. The simulation of cell A was performed at a current density of 1 A cm^{-2} in H_2 humidified with 40% H_2O as fuel at 1023 K to approximate the conditions in the central part of the stack tested in the experiment. For cell B, the simulation was performed at a current density of -1 A cm^{-2} in H_2 humidified with 50% H_2O as fuel at 1073 K, as in the single-cell experiment. The corresponding 3D distributions of the ionic electrochemical potential in YSZ, the electronic potential in Ni, the specified H_2 partial pressure in pore, and the ionic and electronic current densities averaged over the cross-section along the x-axis are shown in Figure 3. The effective thickness of the HFL in both cells was defined as the thickness of HFL from the electrolyte in which 90% of the total electrochemical electronic current is generated. It is clearly seen that the effective thickness of the HFL in cell A is much thinner than cell B, which can be attributed to a much larger TPB density. The corresponding 3D multi-physics field data was then extracted from the adaptive tetrahedral meshes nodes and projected onto the corresponding OP matrices utilized as multi-physical conditions in the PF modeling to update the microstructure of the hydrogen electrode.

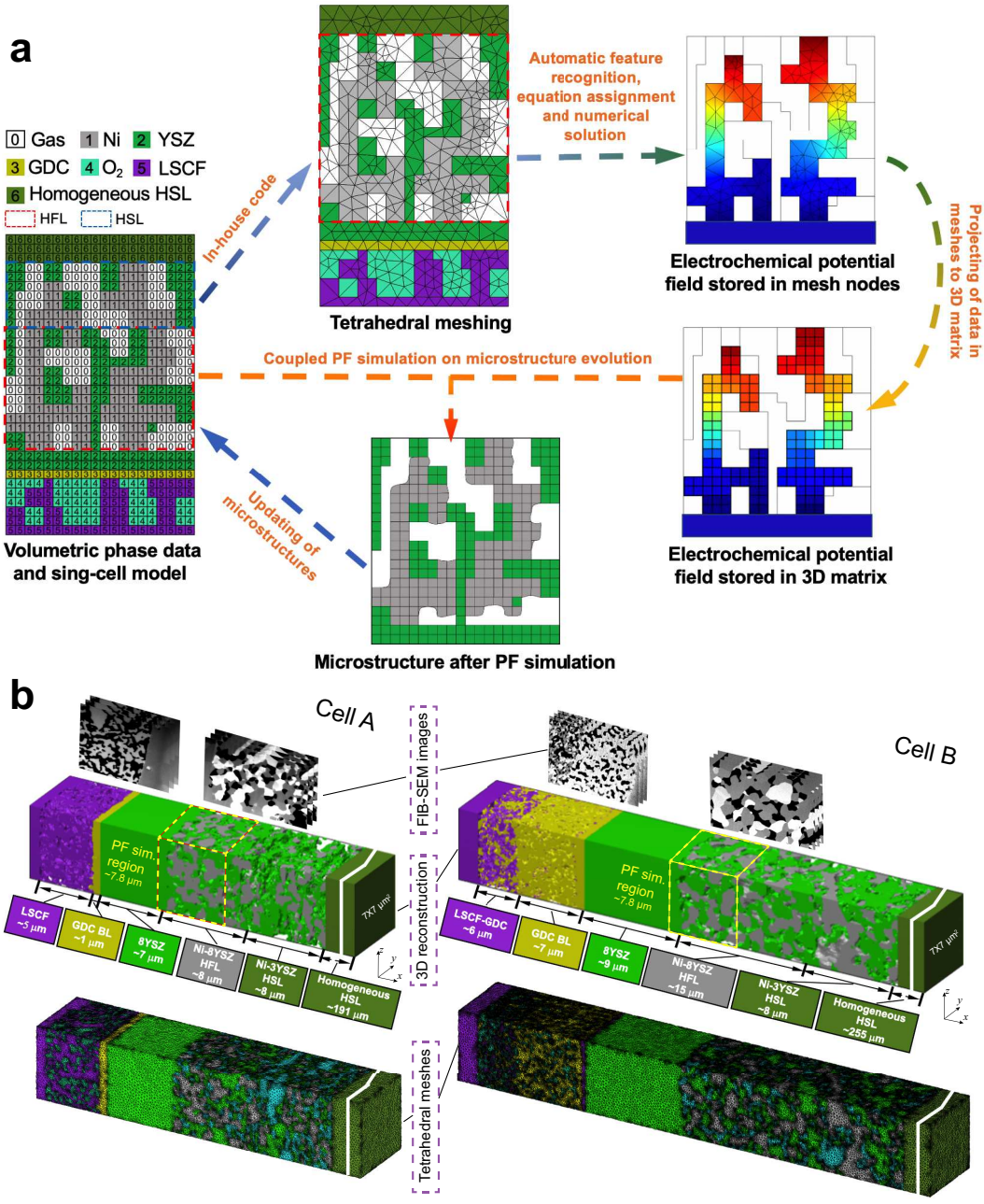

Figure 2: (a) Schematic diagram of the integrated modeling. (b) 3D reconstructions and the corresponding tetragonal meshes of the microstructures of cells A and B in single-cell scale before operation.

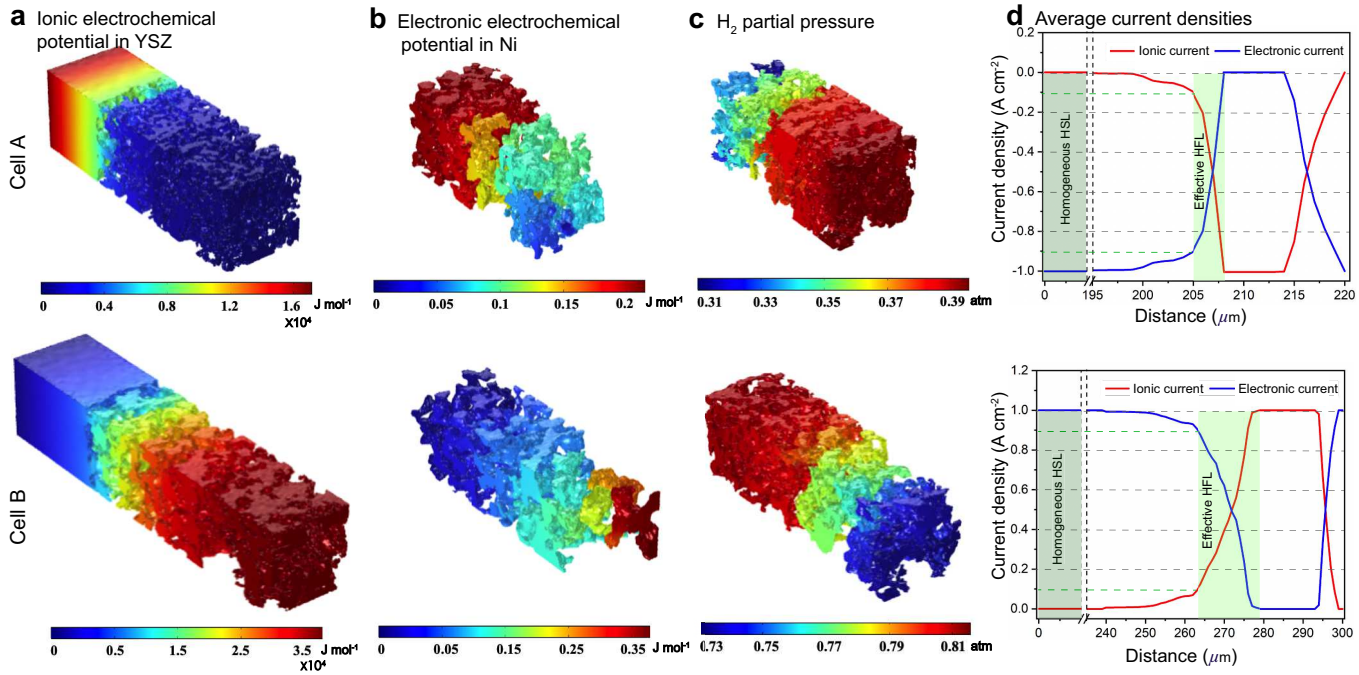

Figure 3: The 3D distributions of (a) ionic electrochemical potential in YSZ, (b) electronic electrochemical potential in Ni, (c) specified H_2 partial pressure in pore and (d) the corresponding cross-section averaged ionic and electronic current densities along the x-axis for cells A and B.

3.3. PF simulations

For PF modeling, the phenomenological parameters in Eq. (8) were calibrated by performing PF simulations on a simplified system of a polycrystalline Ni block bonded to a YSZ substrate, as shown in Fig. 4(a)-(c). The Ni-YSZ system was assumed to be exposed to a uniform gas environment. In the subsequent simulations, the effect of electromigration on Ni caused by electronic current was neglected to calibrate the coefficients by fitting the simulation results to the theoretical values of the contact angle θ.

In our previous work, θ of Ni bonded on YSZ surface in a certain gas environment was correlated with the change of Ni surface tension, which can be modified by oxygen adsorption [19]. It was demonstrated that the change of θ at TPBs can be attributed to the variation of H_2O partial pressure, assuming a constant work of adhesion at the Ni-YSZ interface. Based on the approximation of the Ni surface tension using the

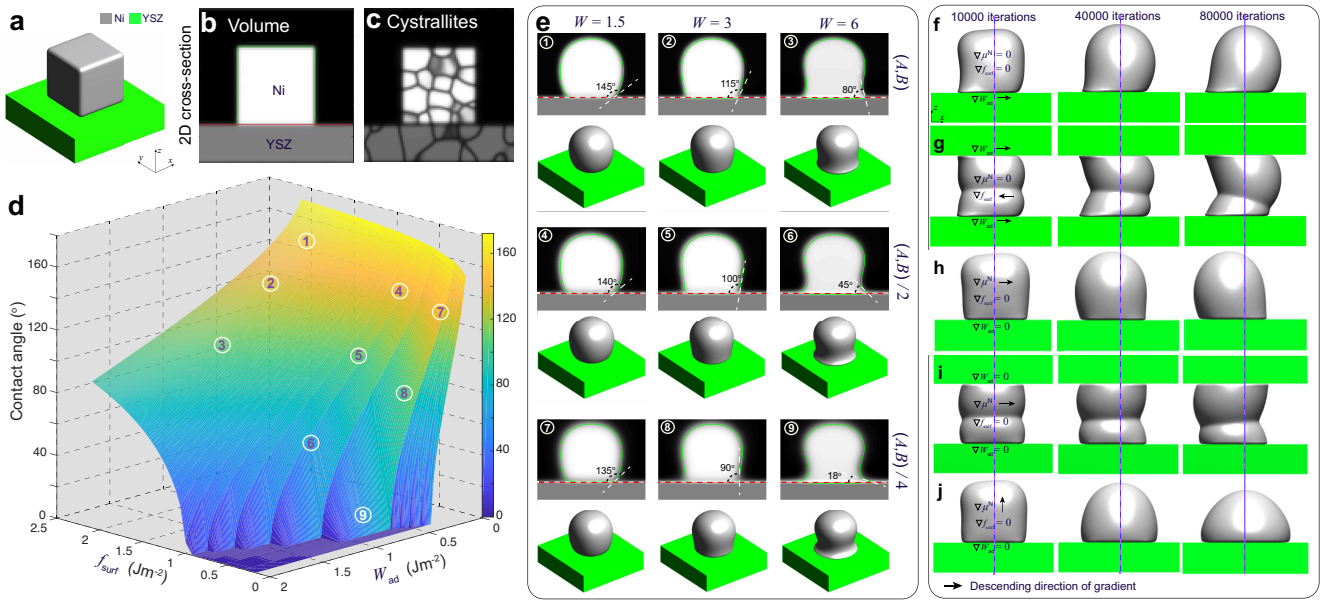

Figure 4: (a) 3D image of Ni block bonded on YSZ substrate and the corresponding 2D cross-section images of (b) phase volume and (c) crystallites. (d) Theoretical contact angle versus surface energy and adhesion work. PF simulation results (e) with different combinations of surface energy and adhesion work, (f) of 3D Ni morphological changes under different gradient conditions.

surface energy f_{surf}, the work of adhesion W_{ad} was correlated with θ and f_{surf} as

$$W_{\mathrm{ad}} = f_{\mathrm{surf}}(1 + \cos\theta). \tag{1}$$

The surface energy of Ni f_{surf} can be calculated as

$$f_{\mathrm{surf}} = f_{\mathrm{surf}}^{\mathrm{p}} - \Gamma^{0} RT \ln\left(1 + K_{\mathrm{a}} a_{\mathrm{O}}\right), \tag{2}$$

where $f_{\mathrm{surf}}^{\mathrm{p}}$ is the surface energy of pure Ni without oxygen adsorption, R is the gas constant, Γ^{0} is the saturated coverage of oxygen adsorption on the Ni surface, and K_{a} is the oxygen adsorption coefficient independent of surface adsorption. a_{O} is the activity of oxygen adsorbed on the surface, which correlates with the local oxygen partial pressure in the bulk gas and can be equated with an atomic percentage (at. %) as $a_{\mathrm{O}} = 2.38 \times 10^{-4} \left(\frac{P_{\mathrm{O_2}}}{P}\right)^{0.5} \exp\left(\frac{1.82\times10^{5}}{RT}\right)$. P_{atm} is the atmospheric pressure and $P_{\mathrm{O_2}}$ is the partial pressure of oxygen, which can be equilibrated by the partial pressure of humidity $P_{\mathrm{H_2O}}$ as follows:

$P_{O_2} = \frac{1}{K_H}\left(\frac{P_{H_2O}}{1-P_{H_2O}}\right)$, where K_H is the equilibrium constant at a conventional SOC operating temperature of T. Details of the parameters can be referred to Ref. [19]. Based on the FE simulation results, the local Ni surface energy can thus be calculated using the P_{H_2O} from the adjacent gas atmosphere.

The work of adhesion W_{ad} at Ni-YSZ interface can be predicted by a Boltzmann expression as [34]

$$W_{ad} = -\frac{n_p}{\Omega_O}E_{vDW} - \frac{n_c}{2\Omega_O}\Delta G_F^\circ, \tag{3}$$

where n_p and n_c are the fractions of physically and chemically bond sites, respectively. Ω_O is the interfacial molar area of YSZ. ΔG_F° is the standard molar Gibbs free energy of the formation of NiO at T, which is calculated using an empirical formula as $\Delta G_F^\circ = -239885 + 122.350T - 4.584T\ln T$ [35]. E_{VDW} is the energy of the Ni-O-Van der Waals pair interaction, which is defined as [36]

$$E_{VDW} = -\frac{3}{2}\frac{\alpha_N\alpha_O}{d^6}\cdot\frac{I_N I_O}{I_N + I_O}., \tag{4}$$

where α_N, α_O, I_N, and I_O are the polarisabilities and ionization potentials of Ni and oxygen ions, respectively. d is the separation distance of the Van der Waals Ni-O bond. The ionic contribution to the bonding as given in the second term of Eq. (3) is much larger than the Van der Waals contribution in the first term, indicating that the Ni-O interaction at a Ni-YSZ interface is terminated by an oxygen plane, and the density of on-top Ni-O ionic bonds across the interface stabilizes the Ni-YSZ interface and dominates W_{ad}. To obtain the values of n_p and n_c, molecular dynamic (MD) simulations were performed to investigate the bonding state at Ni-YSZ interfaces with different vacancy concentrations in YSZ. Details of the simulations can be found in the supplementary materials. With the systematic summary of the MD simulation results, the fraction of Ni-O chemical bonds n_c was correlated with the oxygen vacancy fraction x_V in the oxygen sub-lattice of YSZ surface in a linear relationship, as shown in Fig. 5(a).

According to the work of Hendriks et al. [37], the vacancy concentration on YSZ surface increases with

increasing overpotential and reached a temperature-dependent maximum. The behavior can be understood under the assumption that only a fraction of the oxygen sub-lattice is available for oxygen vacancy distribution, which can be affected by the overpotential at a specific temperature and composition. Thus, the oxygen vacancy fractions in YSZ at Ni-YSZ interfaces during operation in FC or EC mode may be affected by the local overpotential. With variations in the overpotential, the oxygen vacancy fraction in a near-surface YSZ layer can be predicted as

$$x_{\mathrm{V}} = \frac{x_{\mathrm{V}}^{\max} x_{\mathrm{V}}^{\mathrm{bulk}} \exp\left(-z_{\mathrm{V}} e\varphi / k_{\mathrm{B}} T\right)}{x_{\mathrm{V}}^{\max} + x_{\mathrm{V}}^{\mathrm{bulk}} \left[\exp\left(-z_{\mathrm{V}} e\varphi / k_{\mathrm{B}} T\right) - 1\right]}, \tag{5}$$

where φ is the local activation overpotential, z_{V} is the formal charge of an oxygen vacancy, k_{B} is the Boltzmann constant, and x_{V}^{0} is a reference oxygen vacancy fraction at zero overpotential, which is equal to the bulk oxygen vacancy concentration determined by the level of yttria doping in YSZ. The temperature-dependent maximum oxygen vacancy fraction $x_{\mathrm{V}}^{\max}$ was fitted to an Arrhenius-type empirical equation as $x_{\mathrm{V}}^{\max} = C_0 \exp\left(-E/k_{\mathrm{B}}T\right)$, where E and C_0 are constants at a given temperature T [37]. Based on Eqs. (3) and (5), W_{ad} at the Ni-YSZ interface can thus be correlated with the local overpotential during operation in any mode, as shown in Fig. 5(b). It is seen that W_{ad} can be largely decreased with decreasing overpotential. Conversely, increasing overpotential leads to a limited increase in W_{ad}. Based on the FE simulation results, the local overpotential can thus be used to calculate W_{ad} at the Ni-YSZ interface.

Different from our previous work [19], the influences of f_{surf} and W_{ad} were considered simultaneously in PF simulations. According to Eq. (1), the theoretical contact angle is correlated with f_{surf} and W_{ad}, as shown in Fig. 4(d). The phenomenological parameters W, A and B were tuned to reproduce the theoretical values of the contact angle. The variation in f_{surf} was controlled by multiplying A and B by a common factor of $f_{\mathrm{surf}}/f_{\mathrm{surf}}^{0}$, where f_{surf}^{0} is a reference surface energy [19]. A tuning function of $W = -9.35W_{\mathrm{ad}} + 4.69$ was extrapolated to control the variation in W_{ad} by setting a reference contact angle under OCV to 115° [14], and another contact angle under high polarization $\varphi = 0.1$ V to 18°, as shown in Fig. S0 in the supplementary materials [21]. After substituting the given parameters for the environmental conditions into Eqs. (2) to (5), the relevant phenomenological parameters reflecting the changes in f_{surf} and W_{ad} can be

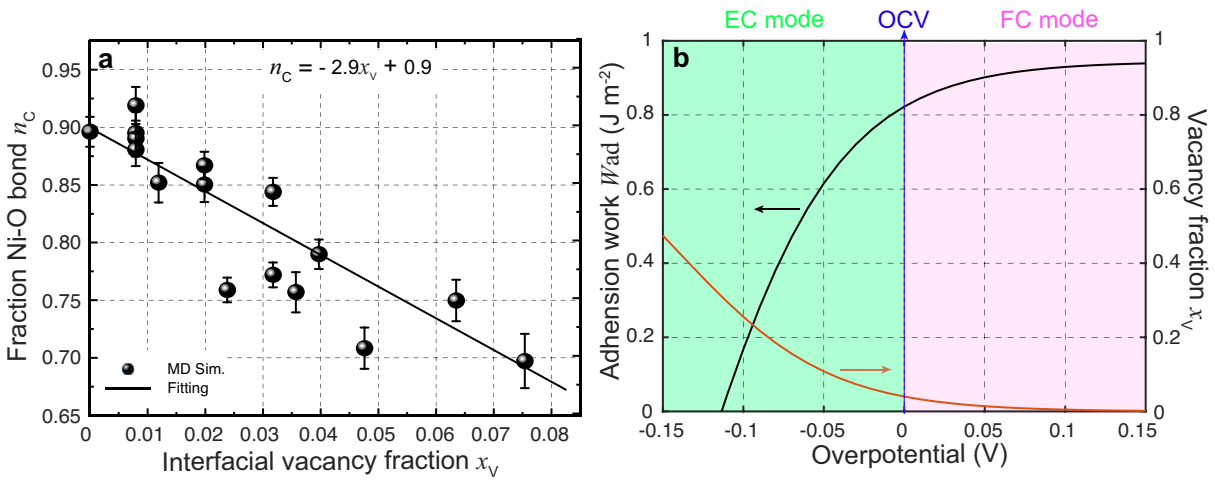

Figure 5: (a) Ionic Ni-O bonds fraction against YSZ surface vacancy fraction. (b) Adhesion work against overpotential predicted using Eq. (3)

obtained for the PF simulations. The PF simulation results of the morphological changes of Ni and the corresponding θ with different combinations of W, A and B are shown in Fig. 4(e). Each simulation was terminated after 80000 iterations to ensure that the Ni morphology reached an equilibrium state. The initial crystallographic orientations of both Ni and YSZ were generated from random initial OPs [20]. It can be clearly seen that theoretical θ, as shown in Fig. 4(d), can be reproduced using different combinations of the phenomenological parameters.

The observations in our previous work indicated that current plays an major role in driving Ni migration, while the contribution of the gas diffusion pathway is minor [14]. The Ni-YSZ contact angle gradient caused by the current could play an important role in driving the Ni surface diffusion in different gas environments. To verify the influence of the contact angle gradient along the Ni-YSZ interface, the simplified PF simulations were rerun by introducing continuous gradients for both f_{surf} and W_{ad} along the x-axis by $\nabla W = -0.01/\text{voxel}$ and $\nabla\left(f_{\text{surf}}/{f^0}_{\text{surf}}\right) = 0.01/\text{voxel}$, while $W = 4$ and $\left(f_{\text{surf}}/{f^0}_{\text{surf}}\right) = 0.75$ were set at the center indicated by the dashed line, as shown in Fig. 4(f) and (g). It can be seen that a gradient in the Ni-YSZ contact angle led to Ni redistribution with limited local migration before the contact angles reached the equilibrium state. The gradients in both f_{surf} and W_{ad} cannot cause continuous Ni migration

with different constrains from the YSZ surfaces.

Our previous work [20] reported the in-situ observations on the continuous spreading of Ni at TPBs in Ni-film electrodes under high anodic polarization using a high-resolution 3D laser scanning confocal microscope. It is clearly seen that the current PF model cannot reproduce the phenomenon of continuous Ni spreading without considering another driving force acting on the Ni phase. After introducing an electrochemical potential gradient on Ni by setting $\nabla\left(\frac{N_a|e|Z^*\mu}{F\Delta f}\mu\right) = 0.01/\text{voxel}$ along different axes, without considering the gradients of f_{surf} and W_{ad}, the PF simulations were performed with different combinations of boundary conditions, as shown in Fig. 4(h) and (i). It can be clearly seen that a continuous translation of the entire Ni along the YSZ surface can be simulated with deformation. When an electrochemical potential gradient is applied along the z-axis on Ni in the simulation, a continuous accumulation of Ni at the YSZ surface can be simulated, as shown in Fig. 4(j). The results show that the continuous migration of Ni under the complex multi-physics coupled influences in both FC and EC modes cannot be reproduced in simulations considering only gradients in f_{surf} and W_{ad}. After a limited range of the redistribution of Ni at the TPBs, the migration stops when the contact angles reach the equilibrium state. Thus, the electrochemical potential gradient induced by the current in the Ni phase is the key factor determining the continuous Ni migration in opposite directions in FC and EC modes in hydrogen electrodes.

To simulate the microstructure evolutions of the hydrogen electrodes in HFLs for cells A and B, the data of the multi-physics fields, as shown in Fig. 3, was first extracted from the nodes of the adaptive tetrahedral meshes and projected onto the corresponding OP matrices. The OP matrices were then used as multi-physical conditions in subsequent PF simulations to control the relevant phenomenological parameters as mentioned above. The PF simulations were then performed based on the reconstruction regions of cells A and B, as indicated in Fig. 2, to update the microstructures. Theoretically, the multi-physical conditions need to be updated after each iteration in a PF simulation, whereas in this work, the update was performed only after every 2000 iterations in the PF simulation to save computational resources given the time-consuming

and costly nature of the integrated simulation. Within the limits of our current computational power, the simulation of cell A was terminated after 46000 iterations, while the simulation of cell B was terminated after 32000 iterations according to the different temperatures to achieve the convergence of the simulations. With the same dimensionless time, the simulations of the microstructure evolutions were also performed under OCV conditions for cells A and B for comparison. The 3D microstructure and the corresponding 2D cross-sectional images of the HFLs in cells A and B before and after the PF simulations in different modes are shown in Fig. 6. It can be clearly seen that the microstructures of both cases under OCV conditions retained most of their original microstructure morphologies. During the simulations, only obvious crystal grain growth and coarsening of Ni are observed, which together change the morphology of the microstructures to a very limited extent under the constraints of the YSZ network. In the simulation of cell A operated in FC mode, significant Ni migration toward the electrolyte could be observed after simulation, as shown in Fig. 6(b). In contrast, Ni migration away from the electrolyte can be observed after the simulation of cell B in EC mode, as shown in Fig. 6(e). In both cases, the extent of Ni migration was much higher at a location closer to the electrolyte, which can be attributed to the larger gradients in current density, as shown in Fig. 3(d). No obvious Ni migration phenomena are observed in the region far from the electrolyte, as shown in the cross-sectional images.

To investigate Ni migration quantitatively, specific cross-section-averaged Ni fraction distributions along the x-axis were calculated as $\int_0^{y_{\max}} \int_0^{z_{\max}} \frac{g(\phi)}{y_{\max} z_{\max}} dydz$ and plotted after the simulations for cells A and B, as shown in Fig. 6(g) and (h). Compared to the reference Ni fraction distributions before the simulations, it is clear that Ni migrates toward the electrolyte when simulating FC mode for cell A, while Ni migrates away from the electrolyte when simulating EC mode for cell B. Under OCV, both cells show almost no redistribution of Ni after the simulations, compared to the initial microstructure. For comparison, two other simulations were performed without considering the gradients of the electrochemical potential in Ni for cells A and B. Similar to the cases under OCV, almost no migration of Ni can be observed after the simulations, which again proves that the electromigration driving force caused by the gradient of electrochemical poten-

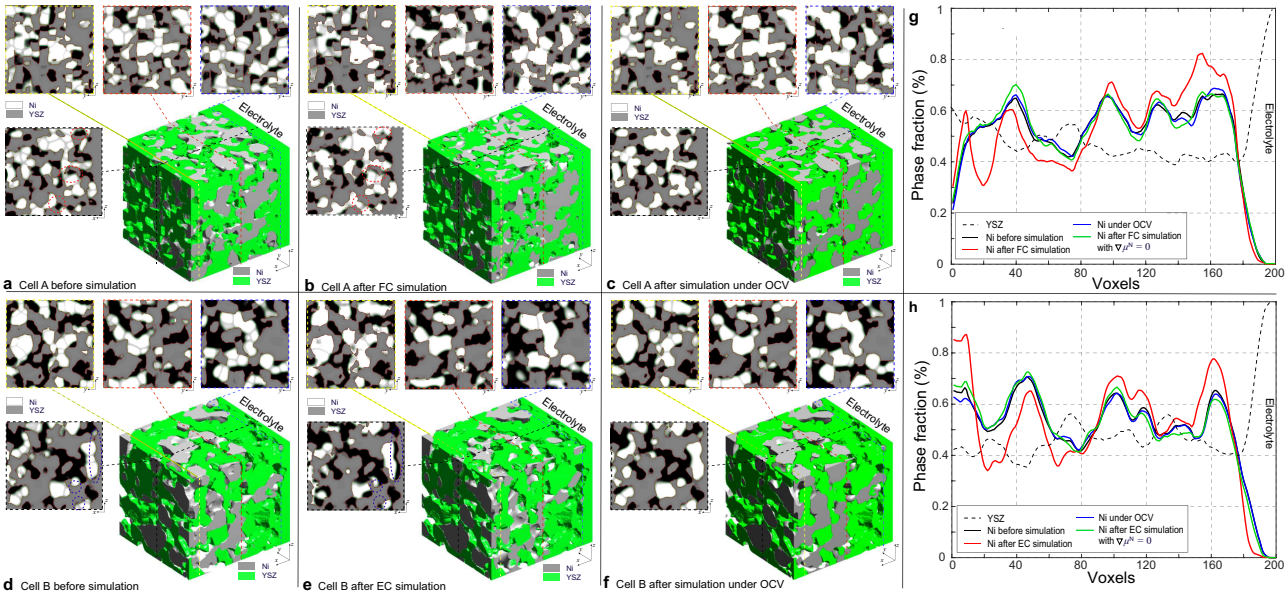

Figure 6: 3D microstructure and the corresponding 2D cross-section images of the HFLs in cell A (a) before and (b) after the simulations of FC operation, and (c) under OCV condition, and cell B (d) before and (e) after the simulations of EC operation and (f) under OCV condition. The corresponding specific cross-section averaged Ni fraction distributions along z-axis for cells (g) A and (h) B.

tial in Ni plays an important role. It is thus known that the change of the contact angle leads to only limited local redistribution of Ni. The experimental observations in the FC and EC modes, as shown in Fig. 1(b) and (d), were well reproduced in the integrated simulations performed under the unique framework, taking into account the dynamic influences of multi-physics coupling effect.

3.4. Case study of the integrated modeling

Ovtar et al. [6] reported that infiltration of nano-sized GDC particles into the conventional Ni-YSZ hydrogen electrode drastically reduced the degradation rate of SOEC performance at high current density. Unlike the bare Ni-YSZ electrode, no contact loss was observed at the Ni-YSZ interface during long-term operation. The lower degradation rate of the hydrogen electrode infiltrated with GDC nanoparticles was attributed to the enlarged active sites compared to the conventional TPBs, which can increase the steam splitting rate and reduce the local overpotential. According to the integrated modeling proposed in this work, a smaller local overpotential leads to a drastic increase in W_{ad}, as shown in Fig. 5(b), which leads

to an enhancement of the Ni-YSZ interface and inhibits Ni migration. At the same time, the Ni surface energy can be reduced by increasing the local concentration of humidity and decreasing the thickness of the active HFL. To quantify the subsequent comprehensive effect caused by the change in overpotential, another simulation was performed on cell B in EC mode, where the exchange current density $i_{0,\mathrm{TPB,fuel}}$ was doubled in Eq. (5).

The simulation was performed for cell B under the identical conditions as described in the previous case shown in Fig. 3. The corresponding 3D distributions of the ionic electrochemical potential in YSZ, the electronic potential in Ni, the specified H_2 partial pressure in the pore, and the ionic and electronic current densities averaged over the cross-section along the x-axis are shown in Fig. 7(a)-(c). Compared to Fig. 3, it is clearly seen that the effective thickness of HFL has decreased from about 15 μm to about 10 μm, following the obvious decrease in the local H_2 partial pressure, which can strongly reduce the surface energy of Ni and thus the local contact angle. The much lower ionic electrochemical potential in YSZ confirmed the prediction of the smaller local overpotential. Therefore, it is reasonable to predict a lower migration rate of Ni with the increase in W_{ad}, as shown in Fig. 7(d).

The subsequent PF simulation was performed based on the condition matrices extracted from the 3D FE simulation results as described previously. Considering the constraining effect of the infiltrated GDC nanoparticles on the Ni surface, the mobility function of the Ni phase was modified by setting $M^*_{\mathrm{surf}} = 0.4$ in the PF simulation without importing the actual GDC nanoparticle morphology into the 3D reconstruction. The 2D cross-sectional images of the HFLs in cell B after the PF simulation are shown in Fig. 7(e). Compared with the initial microstructure shown in Fig. 6(d), it is clear that the similar phenomena of obvious crystal grain growth and coarsening of Ni are observed, while Ni migration from the electrolyte was suppressed to some extent by the stronger bonding at the Ni-YSZ interface. The distributions of Ni fraction along the x-axis after the simulations with the original $i_{0,\mathrm{TPB,fuel}}$ and $2i_{0,\mathrm{TPB,fuel}}$, as shown in Fig. 7(f), reflect the extent to which Ni migration is inhibited. The inhibition of Ni migration can also be attributed

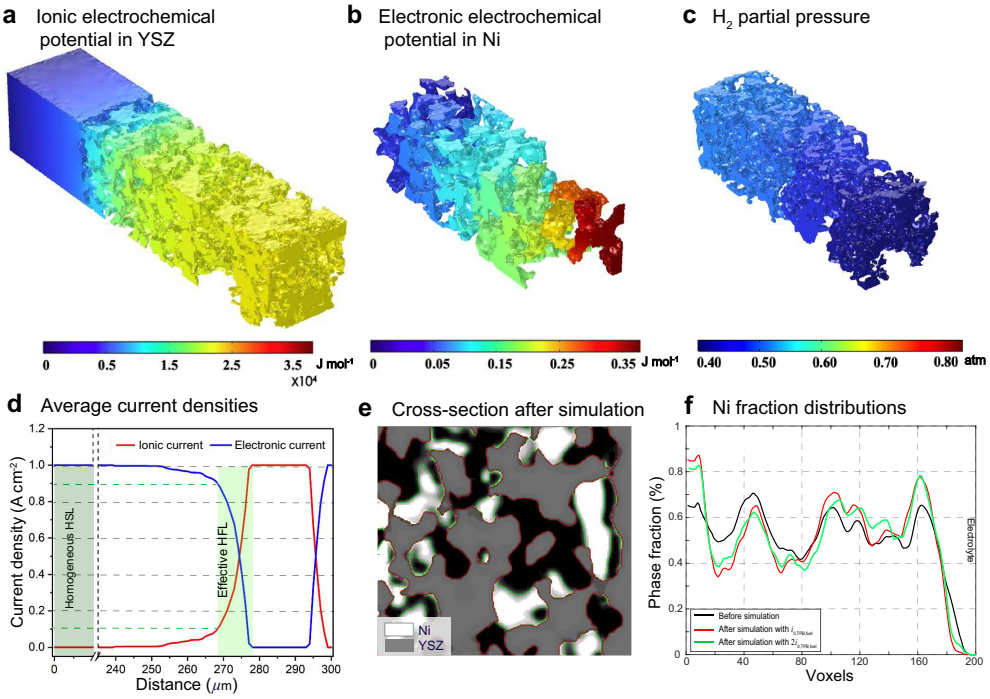

Figure 7: The 3D distributions of (a) ionic electrochemical potential in YSZ, (b) electronic electrochemical potential in Ni, (c) specified H_2 partial pressure in pore and (d) the corresponding cross-section averaged ionic and electronic current densities along the x-axis for cell B with $i_{0,\mathrm{TPB,fuel}}$ doubled. (e) 2D cross-section images of the HFLs in B after the simulation of EC operation, and (f) the corresponding specific cross-section averaged Ni fraction distributions along z-axis.

to the thickness of the effective HFL, which was narrowed by about 30%, as shown in Fig. 7(d), which limits the electromigration driving force within a thinner region of the HFL. It is expected that the phenomenon may become more evident after prolonged operation. Thus, the simulation results theoretically explain the positive effect caused by the infiltration of GDC nanoparticles into the Ni-YSZ hydrogen electrode at high current density [6].

Due to limited computational resources, current simulations of microstructural evolution have been limited to finite time and spatial scales. In future research, larger scale computations over multiple scales and long-term operation can be achieved by improving the relevant algorithms. In addition to the study of Ni migration in hydrogen electrodes, the integrated modeling proposed can also be flexible and open to study the degradation mechanisms of electrolyte and air electrode for SOCs. The current multi-physics coupled full cell model can be further developed for a specific combination of different microstructures to study the comprehensive degradation of SOC life cycle performance in different modes, which could provide the opportunity for revolutionary microstructure investigation and optimization for fuel cells, batteries and other relevant fields.

4. Conclusions

SOCs are clean, efficient, reversible energy conversion solutions that have great potential for a wide range of applications. To fully realize this potential, issues related to improving the durability and lifetime of these systems need to be addressed. In this work, we investigated the phenomena of Ni migration in the hydrogen electrodes of SOCs during operation in the FC and EC modes. An integrated model was developed based on the real 3D microstructures reconstructed at the single-cell scale using the FIB-SEM dual-beam technique. The model linked the FE multi-physics coupled heterogeneous single-cell model with the PF simulations of microstructure evolution by projecting the multi-physical field data from tetragonal meshes onto OPs matrices to simulate the morphological changes of Ni, taking into account the complex

multi-physics coupling effects. The FE model was verified by the experimental measurements in the FC and EC modes under the identical framework. The PF simulation results of the morphological changes in the HFLs of different hydrogen electrodes show that, in addition to conventional coarsening and interfacial energies, Ni migration driven by the electrochemical potential gradient induced by the current plays an important role in Ni migration during operation in the FC and EC modes. The integrated model was also applied in predicting the positive effect of the infiltration of GDC nanoparticles into the Ni-YSZ hydrogen electrode to improve the durability during the operation in EC mode. The simulation results agreed well with the experimental observations, demonstrating the potential of the integrated model in improving the durability of SOCs.

Acknowledgments

The authors acknowledge the funding supported by Guangdong Basic and Applied Basic Research Foundation, China (2023A1515011003), Shenzhen Science and Technology Innovation Commission (JCYJ20210324120404013), Shenzhen Science and Technology Program, China (GJHZ20210705141401004), the Talent Recruitment Project of Guandong Province (2019QN01G098) and the National Natural Science Foundation of China (Nos. 11932005; 52102244).

Declaration of Competing Interest

The authors declare that they have no known competing financial interests or personal relationships that could have appeared to influence the work reported in this paper.

References

References

[1] A. Hauch, R. Kungas, P. Blennow, A.B. Hansen, J.B. Hansen, B.V. Mathiesen, and M.B. Mogensen. Recent advances in solid oxide cell technology for electrolysis. *Science*, 370, 2020.

[2] J. T. S. Irvine, D. Neagu, M. C. Verbraeken, C. Chatzichristodoulou, C. Graves, and M. B. Mogensen. Evolution of the electrochemical interface in high-temperature fuel cells and electrolysers. *Nat. Energy*, 1:15014, 2016.

[3] C. Graves, S. D. Ebbesen, S. H. Jensen, S. B. Simonsen, and M. B. Mogensen. Eliminating degradation in solid oxide electrochemical cells by reversible operation. *Nat. Mater*, 14:239–244, 2015.

[4] S. D. Ebbesen, S. H. Jensen, A. Hauch, and M. B. Mogensen. High temperature electrolysis in alkaline cells, solid proton conducting cells, and solid oxide cells. *Chemical Reviews*, 114:10697–10734, 2014.

[5] M. B. Mogensen, M. Chen, H. L. Frandsen, C. Graves, J. B. Hansen, K. V. Hansen, A. Hauch, T. Jacobsen, S. H. Jensen, T. L. Skafte, and X. Sun. Reversible solid-oxide cells for clean and sustainable energy. *Clean Energy*, 3:175–201, 2019.

[6] S. Ovtar, X. Tong, J. J. Bentzen, K. T. S. Thyden, S. B. Simonsen, and M. Chen. Boosting the performance and durability of Ni/YSZ cathode for hydrogen production at high current densities via decoration with nano-sized electrocatalysts. *Nanoscale*, 11:4394–4406, 2019.

[7] X. Tong, S. Ovtar, K. Brodersen, P. V. Hendriksen, and M. Chen. A 4 x 4 cm(2) nanoengineered solid oxide electrolysis cell for efficient and durable hydrogen production. *ACS Appl Mater Interfaces*, 11:25996–26004, 2019.

[8] Y. Su, Z. Zhong, and Z. Jiao. A novel multi-physics coupled heterogeneous single-cell numerical model for solid oxide fuel cell based on 3D microstructure reconstructions. *Energy & Environmental Science*, 15(6):2410–2424, 2022.

[9] X. Sun, P. V. Hendriksen, M. B. Mogensen, and M. Chen. Degradation in solid oxide electrolysis cells during long term testing. *Fuel Cells*, 19(6):740–747, 2023.

[10] M. Chen, Y. L. Liu, J. J. Bentzen, W. Zhang, X. Sun, A. Hauch, Y. Tao, J. R. Bowen, and P. V. Hendriksen. Microstructural degradation of Ni/YSZ electrodes in solid oxide electrolysis cells under high current. *J. Electrochem. Soc.*, 160:F883–F891, 2013.

[11] A. Hauch, K. Brodersen, M. Chen, and M. B. Mogensen. Ni/YSZ electrodes structures optimized for increased electrolysis performance and durability. *Solid State Ionics*, 293:27–36, 2016.

[12] M. P. Hoerlein, M. Riegraf, R. Costa, G. Schiller, and K. A. Friedrich. A parameter study of solid oxide electrolysis cell degradation: Microstructural changes of the fuel electrode. *Electrochim. Acta*, 276:162–175, 2018.

[13] M. B. Mogensen, A. Hauch, X. Sun, M. Chen, Y. Tao, S. D. Ebbesen, K. V. Hansen, and P. V. Hendriksen. Relation between Ni particle shape change and Ni migration in Ni–YSZ electrodes–a hypothesis . *Fuel Cells*, 2017.

[14] Y. Shang, A. L. Smitshuysen, Y. Miao, Y. Liu, X. Tong, P. S. Jorgensen, L. Rorato, J. Laurencin, and M. Chen. 3D microstructural characterization of Ni/yttria stabilized zirconia electrodes in long-term CO2 electrolysis. *J Mater. Chem. A*, 2023.

[15] D. Kennouche, Y. c.K. Chen-Wiegart, J. S. Cronin, J. Wang, and S. A. Barnett. Three-dimensional microstructural evolution of Ni-yttria-stabilized zirconia solid oxide fuel cell anodes at elevated temperatures. *J. Electrochem. Soc.*, 160(9):F1293–F1304, 2013.

[16] E. Lay-Grindler, J. Laurencin, J. Villanova, P. Cloetens, P. Bleuet, A. Mansuy, J. Mougin, and G. Delette. Degradation study by 3D reconstruction of a nickel–yttria stabilized zirconia cathode after high temperature steam electrolysis operation. *J. Power Sources*, 269:927–936, 2014.

[17] N. H. Menzler, D. Sebold, Y. J. Sohn, and S. Zischke. Post-test characterization of a solid oxide fuel cell after more than 10 years of stack testing. *J. Power Sources*, 478, 2020.

[18] M. B. Mogensen, M. Chen, H. L. Frandsen, C. Graves, A. Hauch, P. V. Hendriksen, T. Jacobsen, S. H. Jensen, T. L. Skafte, and X. Sun. Ni migration in solid oxide cell electrodes: Review and revised hypothesis. *Fuel Cells*, pages 415–429, 2021.

[19] Z. Jiao and N. Shikazono. Study on the effects of polarization on local morphological change of nickel at active three-phase-boundary using patterned nickel-film electrode in solid oxide fuel cell anode. *Acta Materialia*, 135:124–131, 2017.

[20] Z. Jiao and N. Shikazono. In operando optical study of active three phase boundary of nickel-yttria stabilized zirconia solid-oxide fuel cell anode under polarization. *J. Power Sources*, 396:119–123, 2018.

[21] Z. Jiao, E. P. Busso, and N. Shikazono. Influence of polarization on the morphological changes of nickel in fuel electrodes of solid oxide cells. *J. Electrochem. Soc.*, 167, 2020.

[22] T-L. Cheng, Y. Lei, Y. Chen, Y. Fan, H. Abernathy, X. Song, and Y.-H. Wen. Oxidation of nickel in solid oxide cells during electrochemical operation: Experimental evidence, theoretical analysis, and an alternative hypothesis on the nickel migration. *J. Power Sources*, 569, 2023.

[23] A. He, J. Gong, and N. Shikazono. Three dimensional electrochemical simulation of solid oxide fuel cell cathode based on microstructure reconstructed by marching cubes method. *J. Power Sources*, 385:91–99, 2018.

[24] K. Matsuzaki, N. Shikazono, and N. Kasagi. Three-dimensional numerical analysis of mixed ionic and electronic conducting cathode reconstructed by focused ion beam scanning electron microscope. *J. Power Sources*, 196:3073–3082, 2011.

[25] T. Carraro, J. Joos, B. Ruger, A. Weber, and E. Ivers-Tiffee. 3D finite element model for reconstructed mixed-conducting cathodes: I. Performance quantification. *Electrochim. Acta*, 77:315–323, 2012.

[26] J. Joos, T. Carraro, A. Weber, and E. Ivers-Tiffee. Reconstruction of porous electrodes by FIB/SEM for detailed microstructure modeling. *J. Power Sources*, 196:7302–7307, 2011.

[27] Q. Li, D. Chai, L. Wang, X. Zhang, and G. Li. Fine three-dimensional simulation of the heterogeneous anode of a solid oxide fuel cell with direct internal reforming. *Chem. Eng. Sci.*, 242, 2021.

[28] M. E. Lynch, D. Ding, W. M. Harris, J. J. Lombardo, G. J. Nelson, and W. K. S. Chiu. Flexible multiphysics simulation of porous electrodes Conformal to 3D reconstructed microstructures. *Nano Energy*, 2:105–115, 2013.

[29] Y. Wang, C. Wu, B. Zu, M. Han, Q. Du, M. Ni, and K. Jiao. Ni migration of Ni-YSZ electrode in solid oxide electrolysis cell: An integrated model study. *J. Power Sources*, 516, 2021.

[30] Y. Lei, T.-L. Cheng, H. Abernathy, W. Epting, T. Kalapos, G. Hackett, and Y. Wen. Phase field simulation of anode microstructure evolution of solid oxide fuel cell through Ni(OH)2 diffusion. *J. Power Sources*, 482:228971, 2021.

[31] Y. Lei, Y.-L. Lee, W. K. Epting, J. H. Mason, T.-L. Cheng, H. Abernathy, G. Hackett, and Y.-H. Wen. Modeling Ni redistribution in the hydrogen electrode of solid oxide cells through Ni(OH)2 diffusion and Ni-YSZ wettability change. *J. Power Sources*, 545:231924, 2022.

[32] L. Rorato, Y. Shang, S. Yang, M. Hubert, K. Couturier, L. Zhang, J. Vulliet, M. Chen, and J. Laurencin. Understanding the Ni Migration in Solid Oxide Cell: A Coupled Experimental and Modeling Approach. *J. Electrochem. Soc.*, 2023. In press.

[33] Z. Jiao and N. Shikazono. Simulation of nickel morphological and crystal structures evolution in solid oxide fuel cell anode using phase field method. *J. Electrochem. Soc.*, 161(5):F577–F582, 2014.

[34] J. M. Howe. Bonding, structure, and properties of metal/ceramic interfaces: Part 1 chemical bonding, chemical reaction, and interfacial structure. *International Materials Reviews*, 38(5):233–256, 1993.

[35] H. Comert and J. N. Pratt. The standard molar Gibbs free energy of formation of NiO from high-temperature e.m.f. measurements. *The Journal of Chemical Thermodynamics*, 16(12):1145–1148, 1984.

[36] D. Chatain, L. Coudurier, and N. Eustathopoulos. Wetting and interfacial bonding in ionocovalent oxide-liquid metal systems. *Revue de Physique Applique*, 23(6):1055–1064, 1988.

[37] M. G.H.M. Hendriks, H. J. M. Bouwmeester J. E. ten Elshof, and H. Verweij. The defect structure of the double layer in yttria-stabilised zirconia. *Solid State Ionics*, 154:467–472, 2002.

[38] W. Q. Wang and Z. Suo. A simulation of electromigration-induced transgranular slits. *J. Appl. Phys.*, 79(5):2394–2403, 1996.

[39] S. B. Liang, C. B. Ke, M. Y. Tan, M. B. Zhou, and X. P. Zhang. Phase field simulation of the microstructural evolution and electromigration-induced phase segregation in line-type Cu/Sn-Bi/Cu solder interconnects. *17th International Conference on Electronic Packaging Technology*, pages 836–840, 2016.

[40] M. Kilo, M. A. Taylor, Ch. Argirusis, G. Borchardt, R. A. Jackson, O. Schulz, M. Martin, and M. Weller. Modeling of cation diffusion in oxygen ion conductors using molecular dynamics. *Solid State Ionics*, 175(1-4):823–827, 2004.

[41] P. Tanasini, M. Cannarozzo, P. Costamagna, A. Faes, J. Van Herle, A. Hessler-Wyser, and C. Comninellis. Experimental and theoretical investigation of degradation mechanisms by particle coarsening in sofc electrodes. *Fuel cells*, 9(5):740–752, 2009.

[42] S. Hara, K. Shikata, N. Shikazono, S. Izumi, and S. Sakai. Monte carlo study on the constraint effect of YSZ phase on Ni sintering in Ni-YSZ composite system. *ECS Transactions*, 57(1):2857–2863, 2013.

[43] P. K. Schelling and S. R. Phillpot. Mechanism of thermal transport in zirconia and yttria-stabilized zirconia by molecular-dynamics simulation. *J. Am. Ceram. Soc.*, 84(12):2997–3007, 2001.

[44] D. M. Beazley, P. S. Lomdahl, N. G-J. R. Giles, and P. Tamayo. Parallel algorithms for short-range molecular dynamics. *Annual Reviews of Computational Physics III*, pages 119–175, 1995.

[45] P. K. Schelling and S. R. Phillpot. ReaxFF reactive force-field modeling of the triple-phase boundary in a solid oxide fuel cell. *J. Phys. Chem. Lett*, 5(22):4039–4043, 2014.

5. Supplementary material

5.1. Experimental Observation of Ni-film Electrode

The patterned Ni-film electrode was prepared by DC Ni sputtering method and operated in FC and EC modes under larger polarization. The morphological changes of Ni around the edge of the Ni-film after operation in 3% humidified H_2 at 800°C for 5 hours are shown in Fig. S0. Further details of the experiments are given in Ref. [1].

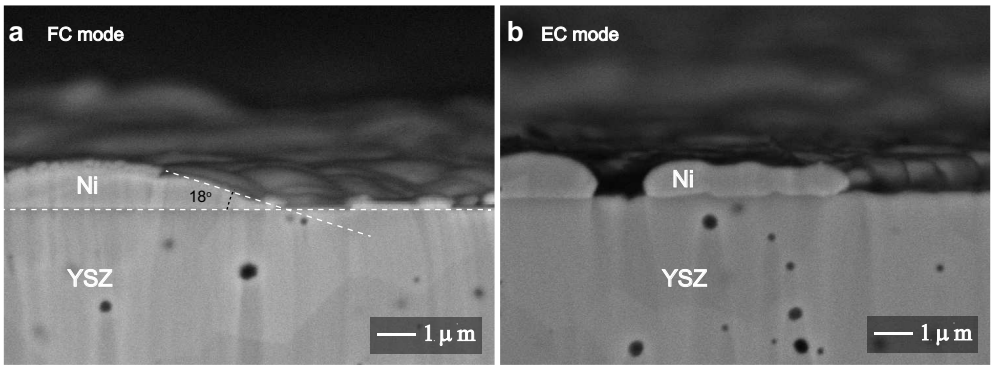

Figure S0: The SEM images of the Ni-YSZ interface cross-sections at the edges of the Ni-film after 5 hours of operation in (a) FC and (b) EC modes.

5.2. Multi-physics coupled FE modeling

To achieve the multi-physics coupled modeling in full-cell scale, the model was built based on a combination of a homogeneous HSL and heterogeneous reconstructions of HSL, HFL, electrolyte, BL, and oxygen electrode. The TPB density, volume fraction, and tortuosity factor obtained based on the 3D reconstruction of the heterogeneous HSL microstructure were used to establish the homogeneous HSL representing the remaining HSL in a large span. The microstructure reconstructions of cells A and B in full-cell scale and the corresponding meshes are shown in Fig. 2(b).

In multi-physics coupled FE modeling, governing equations for the electronic, ionic conduction, and gas

diffusion processes are expressed as

$$\begin{cases} C_{\mathrm{dl}}\frac{\partial}{\partial t}\left(\frac{\tilde{\mu}_{\mathrm{O}^{2-}}}{2F}-\frac{\tilde{\mu}_{\mathrm{e}^-}}{F}\right)-\nabla\cdot\left(\frac{\sigma_{\mathrm{O}^{2-}}}{2F}\nabla\tilde{\mu}_{\mathrm{O}^{2-}}\right)=-i_{\mathrm{reac}} \\ -C_{\mathrm{dl}}\frac{\partial}{\partial t}\left(\frac{\tilde{\mu}_{\mathrm{O}^{2-}}}{2F}-\frac{\tilde{\mu}_{\mathrm{e}^-}}{F}\right)-\nabla\cdot\left(\frac{\sigma_{\mathrm{e}^-}}{F}\nabla\tilde{\mu}_{\mathrm{e}^-}\right)=i_{\mathrm{reac}} \\ \frac{\partial c_j}{\partial t}+\nabla\cdot(D_j\nabla c_j)=s_j,\ \left(s_{\mathrm{H_2}}=\frac{i_{\mathrm{reac}}}{2F},s_{\mathrm{O_2}}=-\frac{i_{\mathrm{reac}}}{4F}\right) \end{cases}, \tag{1}$$

where $\tilde{\mu}_{\mathrm{O}^{2-}}$, $\tilde{\mu}_{\mathrm{e}^-}$, $\sigma_{\mathrm{O}^{2-}}$, and σ_{e^-} represent the electrochemical potentials and conductivities of oxygen ions and electrons, respectively. C_{dl} is the capacitance of the heterogeneous double-layer. The effective double-layer capacitance $C^{\mathrm{eff}}_{\mathrm{dl,HSL}}$ in the HSL can be evaluated as $C^{\mathrm{eff}}_{\mathrm{dl,HSL}}=C^{\mathrm{N/Y}}_{\mathrm{dla}}S_{\mathrm{N/Y}}$, where $S^{\mathrm{N/Y}}$ is the volume-specific Ni-YSZ interfacial area. Thus, the effective oxygen ion conductivity, electron conductivity, and gas diffusion coefficients can be calculated using the corresponding volume fraction V_j and the tortuosity factor τ_j of phase j as

$$\Gamma^{\mathrm{eff}}_j=\frac{V_j}{\tau_j}\Gamma_j\,(\Gamma_j=\sigma_{\mathrm{O}^{2-}},\sigma_{\mathrm{e}^-},D_{\mathrm{H_2,H_2O}},D_{\mathrm{H_2,kn}}). \tag{2}$$

F is the Faraday constant, i_{reac} is the stable Faraday current density associated with the sustained electrochemical reactions at TPBs or double-phase-boundaries (DPBs), c_j is the molar concentration of gas species j, and s_j is the volumetric specific molar consumption rate of gas species j in the electrochemical reactions. The corresponding gas diffusivity D_j can be calculated based on a simplified dust gas model (DGM) as

$$D_j=\left(\frac{1-\alpha y_j}{D_{j,k}}+\frac{1}{D_{j,\mathrm{kn}}}\right)^{-1}, \tag{3}$$

with the binary diffusion coefficient $D_{j,k}$ and the Knudsen diffusion coefficient $D_{j,\mathrm{kn}}$ defined as

$$\begin{cases} D_{j,k}=0.0005956\sqrt{\frac{1}{M_j}+\frac{1}{M_k}}\frac{T^{3/2}}{P_t\Omega_{\mathrm{D}}\zeta^2_{j,k}} \\ D_{j,\mathrm{kn}}=\frac{2}{3}r\sqrt{\frac{8RT}{\pi M_j}} \end{cases}, \tag{4}$$

where M_j is the molecular weight of the gas species j, P_{t} is a constant total pressure, T is a constant temperature, and $\alpha=1-\sqrt{\frac{M_j}{M_k}}$. The intermolecular force constant $\zeta_{j,k}$ was taken as the arithmetic mean of ζ_j and ζ_k. The collision integral is defined as $\Omega_{\mathrm{D}}=1.1336\left(\frac{Tk}{\varepsilon}\right)^{-0.1814}$, where ε is the geometric mean value.

The electrochemical reactions in the hydrogen electrode occur only at Ni-YSZ-pore TPBs, while the electrochemical reactions in the oxygen electrode occur simultaneously at the LSCF-GDC DPBs and LSCF-GDC-pore TPBs. The corresponding local electrochemical reaction current density integrals at the heterogeneous boundary and interface, as well as the current density in the homogeneous HSL, can be calculated using a group of Butler-Volmer equations as

$$\begin{cases} \lim\limits_{\delta S\to 0}\int i_{\mathrm{reac,TPB,fuel}}\mathrm{d}S = i_{0,\mathrm{TPB,a}}\left[\exp\left(\frac{2.0F}{RT}\eta_{\mathrm{act,fuel}}\right)-\exp\left(-\frac{1.0F}{RT}\eta_{\mathrm{act,fuel}}\right)\right] \\ \lim\limits_{\delta S\to 0}\int i_{\mathrm{reac,TPB,O_2}}\mathrm{d}S = i_{0,\mathrm{TPB,O_2}}\left[\exp\left(\frac{2.0F}{RT}\eta_{\mathrm{act,O_2}}\right)-\exp\left(-\frac{2.0F}{RT}\eta_{\mathrm{act,O_2}}\right)\right] \\ \lim\limits_{\delta l\to 0}\int i_{\mathrm{reac,DPB,O_2}}\mathrm{d}l = i_{0,\mathrm{DPB,O_2}}\left[\exp\left(\frac{1.2F}{RT}\eta_{\mathrm{act,O_2}}\right)-\exp\left(-\frac{1.0F}{RT}\eta_{\mathrm{act,O_2}}\right)\right] \\ i_{\mathrm{reac,HSL}} = i_{0,\mathrm{TPB,fuel}}l_{\mathrm{TPB,HSL}}\left[\exp\left(\frac{2.0F}{RT}\eta_{\mathrm{act,fuel}}\right)-\exp\left(-\frac{1.0F}{RT}\eta_{\mathrm{act,fuel}}\right)\right] \end{cases}, \tag{5}$$

where $i_{0,\mathrm{TPB,fuel}}$, $i_{0,\mathrm{TPB,O_2}}$, and $i_{0,\mathrm{DPB,O_2}}$ are exchange-current densities at TPBs in hydrogen electrode, at TPBs and DPBs in oxygen electrode, respectively. $i_{\mathrm{reac,HSL}}$ is the volume specific electrochemical reaction current in the HSL.

5.3. Multi-physics coupled PF modeling

Based on the results of the multi-physics coupled FE simulation, the microstructure evolutions in the Ni-YSZ composite hydrogen electrode during operation in different modes for both cells A and B were simulated using PFM. A unique resolution of $180 \times 200 \times 180$ discrete voxels was used in the simulations, with a length of about 10 voxels belonging to electrolyte and the rest belonged to electrode. Phases Ni and YSZ were introduced in PF modeling using two OPs, i.e. $\phi^{\mathrm{N}}(\boldsymbol{r})$ and $\phi^{\mathrm{Y}}(\boldsymbol{r})$, where $\boldsymbol{r}$ is a spatial parameter. $\phi^{\mathrm{N/Y}}(\boldsymbol{r}) = 1$ was set in solid phase, and $\phi^{\mathrm{N/Y}}(\boldsymbol{r}) = 0$ outside. The pore phase can be determined as $\phi^{\mathrm{P}}(\boldsymbol{r}) = 1 - \phi^{\mathrm{N}} - \phi^{\mathrm{Y}}$. Moreover, the crystallographic orientations in a given solid phase were defined using OPs as $[\eta_1(\boldsymbol{r}), \eta_2(\boldsymbol{r}), \ldots, \eta_q(\boldsymbol{r})] = (\pm 1.0, 0, \ldots, 0), (0, \pm 1.0, \ldots, 0), \cdots (0, 0, \ldots, \pm 1.0)$, where q is the number of crystallographic orientations for both the Ni phase and the YSZ phase, while ± 1.0 indicates two

different crystallographic orientations in one orientation OP. The total free energy of the system can thus be expressed as

$$F = \int_V dV \left\{ \Delta f f_0 \left(\phi^{\mathrm{N}}, \phi^{\mathrm{Y}}, \eta_j^{\mathrm{N}}, \eta_j^{\mathrm{Y}} \right) + \sum_{p=\mathrm{N}}^{\mathrm{Y}} \left[\frac{\kappa_\phi^p}{2} (\nabla \phi^p)^2 + \sum_{j=1}^{q} \frac{\kappa_j^p}{2} \left(\nabla \eta_j^p \right)^2 \right] \right\}, \tag{6}$$

where κ_ϕ^p and κ_j^p are the corresponding coefficients of the gradient energy of the material surface and grain boundary. Thus, the free energy density of the system f_0 is composed of the contributions from the various interfaces and the electromigration driving force on the Ni phase subjected to a current density [38, 39], which is defined as

$$f_0 = \Delta f \left\{ \sum_{p=\mathrm{N}}^{\mathrm{Y}} \left[f_1 \left(\phi^p \right) + \sum_{j=1}^{q} f_2 \left(\phi^p, \eta_j^p \right) + \sum_{j=1}^{q} \sum_{k \neq j}^{q} f_3 \left(\eta_j^p, \eta_k^p \right) \right] + f_4 \left(\phi^{\mathrm{N}}, \phi^{\mathrm{Y}} \right) + f_5 \left(\phi^{\mathrm{N}}, \phi^{\mathrm{Y}} \right) \right\} + f_6 \left(\phi^{\mathrm{N}}, \mu^{\mathrm{N}} \right), \tag{7}$$

where Δf is a common coefficient of the interfacial energy densities and

$$\begin{cases} f_1 \left(\phi^x \right) = -\left(A/2 \right) \left(\phi^x - \phi^m \right)^2 + \left(B/4 \right) \left(\phi^x - \phi^m \right)^4 + \left(D/4 \right) \left(\phi^x - \phi^0 \right)^4 \\ f_2 \left(\phi^x, \eta_j^x \right) = -\left(\gamma/2 \right) \left(\phi^x - \phi^0 \right)^2 \left(\eta_j^x \right)^2 + \left(\gamma/4 \right) \left(\eta_j^x \right)^4 \\ f_3 \left(\eta_j, \eta_k \right) = \left(\varepsilon_{jk}/2 \right) \left(\eta_j \right)^2 \left(\eta_k \right)^2 \\ f_4 \left(\phi^x, \phi^y \right) = \left(\lambda/2 \right) \left(\phi^x \right)^2 \left(\phi^y \right)^2 \\ f_5 \left(\phi^x, \phi^y \right) = -W \phi^x |\nabla \phi^y|^2 \\ f_6 \left(\phi^x, \mu^x \right) = -H \phi^x \mu^x \end{cases}, \tag{8}$$

where f_1, f_2, f_3 and f_4 correspond to a volume fraction-dependent double-well potential function, the mutual coupling effects among the volume fractions and the crystallographic orientations of different phases, respectively. f_5 denotes a term related to the wettability of Ni on YSZ. The coefficient H in f_6, defined as $H = \frac{N_a |e| Z^*}{F}$, is a fixed value describing an electromigration-induced driving force exerted on Ni by the electron wind force along a current driven by an electrochemical potential gradient [38, 39]. N_a is the number of Ni atoms per unit volume, e is the charge of an electron, and Z^* is the effective valence of the

Ni atom. The driving force can thus be related to the electrochemical potential field μ^{N} generated in the multi-physics coupled FE simulation.

To facilitate the simulation, YSZ was set as a stable phase due to its low diffusion coefficient at the operating temperature [40], which is also consistent with the experimental observation [41]. The conserved Cahn-Hilliard dynamic evolution equation was utilized as the governing equation to predict Ni phase evolution as

$$\frac{\partial \phi^{\mathrm{N}}}{\partial t} = \nabla \cdot \left[M \nabla \left(\frac{\partial f_0}{\partial \phi^{\mathrm{N}}} - \kappa_{\phi}^{\mathrm{N}} \nabla^2 \phi^{\mathrm{N}} \right) \right] \tag{9}$$

where t is time and M is the mobility of Ni phase, which is defined as

$$M = M_{\phi}^{\mathrm{N}} \left[M_{\mathrm{vol}}^{*} h\left(\phi^{\mathrm{N}}\right) + M_{\mathrm{surf}}^{*} \phi^{\mathrm{N}} \left(1 - \phi^{\mathrm{N}}\right) + M_{\mathrm{gb}}^{*} \sum_{j}^{p} \sum_{k \neq j}^{p} \left| \eta_j^{\mathrm{N}} \eta_k^{\mathrm{N}} \right| \right] g\left(1 - \phi^{\mathrm{Y}}\right), \tag{10}$$

where $h\left(x\right) = x^3\left(10 - 15x + 6x^2\right)$, $g\left(x\right) = x^6\left(10x^2 - 15x + 6\right)$ are two interpolation functions used to limit the mobility of Ni in bulk and at Ni-YSZ interface. In addition, M_{ϕ}^{N} is an unknown composition coefficient of Ni under a specific operation conditions, and the dimensionless coefficients $M_{\mathrm{vol}}^{*} = 0.01$, $M_{\mathrm{surf}}^{*} = 4$ and $M_{\mathrm{gb}}^{*} = 0.4$ are related to the bulk, the surface and grain boundary of Ni, respectively.

Based on the Allen-Cahn dynamics evolution equation, non-conserved governing equations of Ni crystal grain growth can be defined as

$$\frac{\partial \eta_j^{\mathrm{N}}}{\partial t} = -L_j \left(\frac{\partial f_0}{\partial \eta_j^{\mathrm{N}}} - \kappa_j^{\mathrm{N}} \nabla^2 \eta_j^{\mathrm{N}} \right); j = 1, 2, \ldots, q \tag{11}$$

where L_j is the mobility of Ni grain boundary. To facilitate the calculation, the value of L_j was assumed to be identical for each crystallographic orientation. The fourier-spectral method was utilized to solve the partial differential equations, and periodic boundary conditions were applied along the three axes in all simulations. The phenomenological parameters in Eq. (8) were chosen as $\phi_m = 0.5$, $\phi_0 = 0$, $A = 1.0$,

$B = 4.0$, $D = 1.0$, $\gamma = 1.0$, $\varepsilon_{jk} = 3.0$, and $\lambda = 1.19$. Gradient coefficients were chosen as $\kappa_\phi^{\mathrm{N}} = 1$, $\kappa_\phi^{\mathrm{Y}} = 0.82$, $\kappa_j^{\mathrm{N}} = 0.71$, and $\kappa_j^{\mathrm{Y}} = 0.52$ [33, 42]. A dimensionless coefficient $H^* = \frac{H\mu_{\max}}{\Delta f}$ was set to 250 in f_6 to control the electromigration driving force. After non-dimensionalizing the other relevant parameters and the governing equations, a semi-implicit scheme was applied to alleviate the time-step constraint without loss of stability or accuracy, with the further details are given in Refs. [20, 33].

5.4. MD Modeling

As a common interfacial combination between Ni and YSZ, the Ni[111]/YSZ[111] interface was chosen as a representative example in the present MD simulations, as shown in Fig. S1. The YSZ model was constructed by randomly replacing Zr^{4+} with Y^{3+} in ZrO_2. To keep the charge neutral, one O^{2+} was randomly deleted in the model when two Zr^{4+} ions were replaced [2]. In addition, the YSZ layer with doping concentration ranging from 1mol% (1YSZ) to 35mol% (35YSZ) was used to investigate the effects of doping concentration on the interfacial bonding properties. The sizes of YSZ and Ni in the Ni-YSZ supercell were chosen so that the lattice mismatch at the interface was less than 3%. Periodic boundary conditions were applied in all directions. A vacuum layer with a thickness of 20 Å was added along the z-axis to avoid the repeated interface caused by periodicity. All simulations were performed in the LAMMPS package [3]. A recently developed ReaxFF potential was used to describe the formation of the Ni-YSZ interface [4], which contains the bond order to describe the formation and breaking of chemical bonds. The ReaxFF potential can well simulate Ni-O bond formation at Ni-YSZ interfaces, which is not possible with conventional potentials. To obtain a stable interface, the Ni-YSZ system was first relaxed at the corresponding temperature using the isothermic-isobaric (NPT) ensemble to relieve the stress, and then switched to the isothermic-isochoric (NVT) ensemble to allow the system to reach a steady state. The binding properties of the Ni-YSZ interfaces were then analyzed.

The stability of the Ni-YSZ interfaces was verified by the convergence of the system energy, as shown in Fig. S2(a). Since the Ni-O bond is the predominant chemical bond at the Ni-YSZ interface, we show in

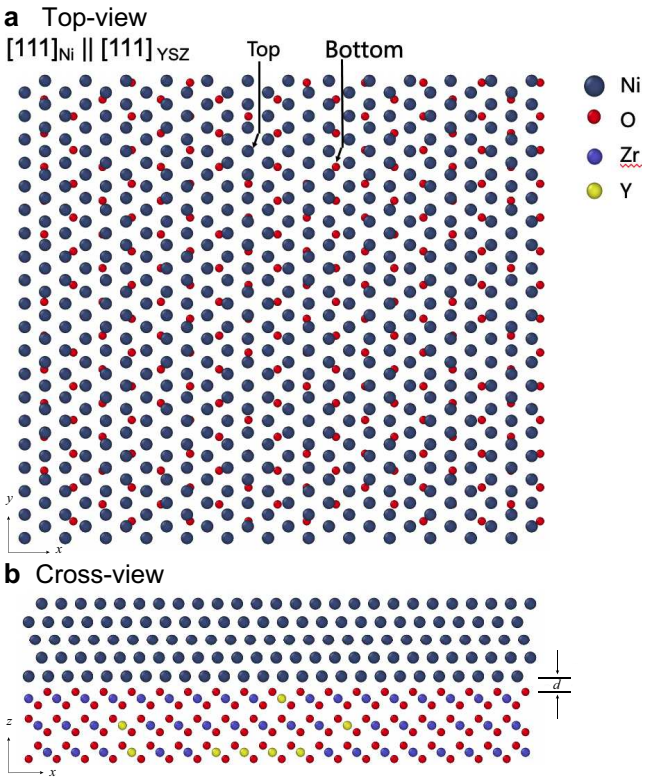

Figure S1: The model of Ni-YSZ interface used in the MD simulation.

Fig. S2(b) the evolution of the interfacial O atoms bonded to Ni atoms during the MD simulations, which was measured as the fraction of the number of bonded O atoms in the total number of O atoms in YSZ surface. It was found that the fraction of O atoms bonded in all Ni-YSZ interface models remained almost unchanged at the end of the MD simulations, which indicates the stability of the Ni-YSZ interfaces obtained. Based on Fig. S2(b), the fractions of bonded O atoms at different Ni-YSZ interfaces with different doping concentrations in YSZ are plotted in Fig. S3(a). It can be seen that the fraction of bonded O atoms decreases from 0.90 in the Ni-1YSZ interface to 0.69 in its Ni-35YSZ counterpart, indicating that the number of Ni-O bonds decreases with the increase of doping concentration. Therefore, it is expected that the bond strength of the Ni-YSZ interface becomes weaker as the doping concentration of YSZ increases. Figure S3(b) shows the defect fraction at the interface of all Ni-YSZ models. It is defined as the ratio between the number of O vacancies in the inner surface of YSZ to the number of O atoms in the perfect ZrO_2 surface. It is found that the interfacial defect fraction of the Ni-YSZ structure generally increases as the doping concentration increases. Thus, the decrease in the number of interfacial O atoms in this process is responsible for the lower number of Ni-O bonds formed at a higher doping concentration.

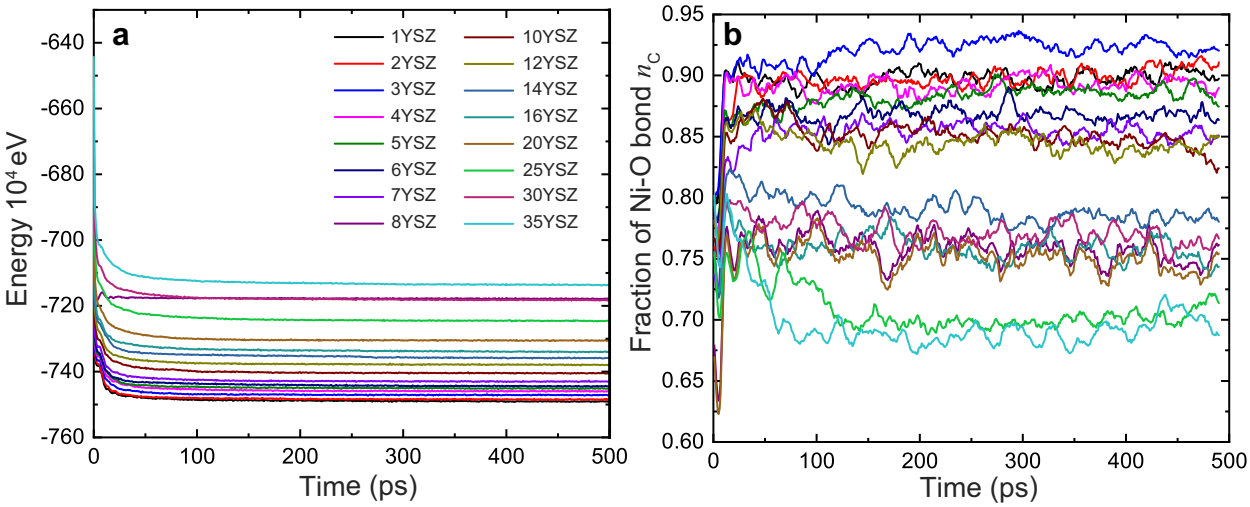

Figure S2: (a) Energy change and (b) evolution of fraction of bonded O atoms during the simulation process.

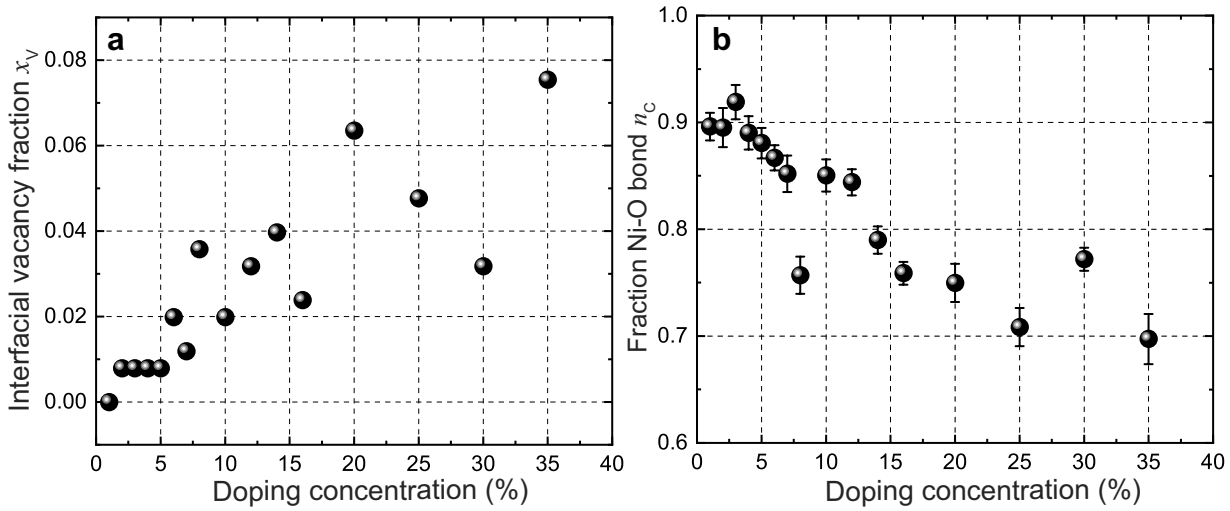

Figure S3: Fractions of (a) bonded O atoms and (b) interfacial defect of YSZ versus yittria-doping concentrations.

References

[1] Z. Jiao and N. Shikazono, Study on the effects of polarization on local morphological change of nickel at active three-phase-boundary using patterned nickel-film electrode in solid oxide fuel cell anode, Acta Materialia, 135 (2017) 124–131.

[2] P. K. Schelling and S. R. Phillpot, Mechanism of Thermal Transport in Zirconia and Yttria-Stabilized Zirconia by Molecular-Dynamics Simulation, Journal of the American Ceramic Society,84(12) (2001) 2997–3007.

[3] D. M. Beazley, P. S. Lomdahl, N. Gronbech-Jensen, et al., Parallel Algorithms for Short-Range Molecular Dynamics, Annual Reviews of Computational Physics III, (1995) 119–175.

[4] B. V. Merinov, J. E. Mueller, A. C. T. Van Duin, et al., ReaxFF Reactive Force-Field Modeling of the Triple-Phase Boundary in a Solid Oxide Fuel Cell, The Journal of Physical Chemistry Letters, 5(22) (2014) 4039–4043.